*nanomaterials*

MDPI

*Article*

# A Low-Cost Electrochemical Cell Sensor Based on MWCNT-COOH/$\alpha$-$Fe_2O_3$ for Toxicity Detection of Drinking Water Disinfection Byproducts

**Ying Liu, Zhipeng Zhang, Yuling Wu, Huan Yang, Jiao Qu and Xiaolin Zhu ***

School of Environment, Northeast Normal University, Changchun 130117, China
* Correspondence: zhuxl668@nenu.edu.cn; Tel.: +86-431-8916-5600; Fax: +86-431-8916-5621

**Abstract:** The disinfection of drinking water is essential for eliminating pathogens and preventing waterborne diseases. However, this process generates various disinfection byproducts (DBPs), which toxicological research indicates can have detrimental effects on living organisms. Moreover, the safety of these DBPs has not been sufficiently assessed, underscoring the need for a comprehensive evaluation of their toxic effects and associated health risks. Compared to traditional methods for studying the toxicity of pollutants, emerging electrochemical sensing technologies offer advantages such as simplicity, speed, and sensitivity, presenting an effective means for toxicity research on pollutants. However, challenges remain in this field, including the need to improve electrode sensitivity and reduce electrode costs. In this study, a pencil graphite electrode (PGE) was modified with carboxylated multi-walled carbon nanotubes (MWCNT-COOH) and nano-iron (III) oxide ($\alpha$-$Fe_2O_3$) to fabricate a low-cost electrode with excellent electrocatalytic performance for cell-active substances. Subsequently, a novel cellular electrochemical sensor was constructed for the sensitive detection of the toxicity of three drinking water DBPs. The half inhibitory concentration ($IC_{50}$) values of 2-chlorophenylacetonitrile (2-CPAN), 3-chlorophenylacetonitrile (3-CPAN), and 4-chlorophenylacetonitrile (4-CPAN) for HepG2 cells were 660.69, 831.76, and 812.83 μM, respectively. This study provides technical support and scientific evidence for the toxicity detection and safety assessment of emerging contaminants.

**Keywords:** biosensor; disinfection byproducts; cytotoxicity; multi-walled carbon nanotubes; nano-iron (III) oxide



Academic Editor: Domenica Tonelli

Received: 13 December 2024
Revised: 15 January 2025
Accepted: 17 January 2025
Published: 20 January 2025

**Citation:** Liu, Y.; Zhang, Z.; Wu, Y.; Yang, H.; Qu, J.; Zhu, X. A Low-Cost Electrochemical Cell Sensor Based on MWCNT-COOH/ $\alpha$-$Fe_2O_3$ for Toxicity Detection of Drinking Water Disinfection Byproducts. *Nanomaterials* **2025**, *15*, 146. https://doi.org/10.3390/nano15020146



## 1. Introduction

Drinking water disinfection is considered one of the greatest public health achievements of the 20th century, as it is vital for eliminating pathogenic microorganisms and preventing the spread of waterborne diseases. However, during disinfection processes, disinfectants react with natural organic matter, anthropogenic pollutants, and inorganic ions present in source water, resulting in the formation of numerous disinfection by-products (DBPs) [1,2]. Since the identification of trihalomethanes (THMs) in 1974, over 700 DBPs have been detected [3,4]. In recent years, a significant increase in the detection of aromatic disinfection by-products in drinking water has been observed. Toxicological studies indicate that these aromatic DBPs generally possess higher levels of cytotoxicity, genotoxicity, developmental toxicity, and growth inhibition when compared to aliphatic DBPs [5]. Chlorochloroacetonitrile is a highly stable aromatic nitrogen-containing compound formed during chlorination and chloramine disinfection processes. It has been

measured in drinking water at concentrations in the ng/L range [6]. Toxicological assessments of 2-chlorophenylacetonitrile (2-CPAN) using Chinese hamster ovary cells have revealed significant toxicity, with 2-CPAN exhibiting toxicity that is 61 times greater than that of regulated trichloromethane [7]. Furthermore, 3-chlorophenylacetonitrile (3-CPAN) and 4-chlorophenylacetonitrile (4-CPAN) have recently been detected in drinking water [8]. Consequently, there is an urgent need for rapid and accurate evaluations of the toxic effects of these DBPs in drinking water.

Traditional methods for assessing the cytotoxicity of environmental pollutants, such as the MTT assay, lactate dehydrogenase (LDH) assay, and flow cytometry, have several limitations, including high costs, complex procedures, and the necessity for staining [9,10]. Therefore, there is a pressing need to develop a rapid, sensitive, cost-effective, non-toxic, and staining-free evaluation method. Recently, an electrochemical approach based on nucleotide metabolism has emerged as a novel technique for detecting the cytotoxicity of pollutants [11]. This method assesses cell viability by measuring the electrochemical signals of nucleotide metabolites, such as guanine and xanthine, which reflect the toxic effects of pollutants on cells [12]. It offers several advantages, including simplicity, speed, non-toxicity, and the absence of labeling [13], thereby showing promise for applications in environmental toxicology research [14]. However, there are currently several issues in this field, including the high cost of electrodes, the need for improved electrode sensitivity, and the relatively complex surface treatment and modification of electrodes. In comparison to commonly used glassy carbon electrodes, lead core electrodes are significantly less expensive, costing approximately one-thousandth as much. Additionally, they offer a wide electrochemical window, ease of modification, and the ability to reduce surface passivation effects [15,16]. To improve the sensitivity of electrochemical detection, it is essential to modify the electrodes with high-performance novel nanomaterials.

Multi-walled carbon nanotubes (MWCNTs) are characterized by a large specific surface area and excellent conductivity, making them widely utilized in the fabrication of electrochemical sensors. Functionalization treatments, such as hydroxylation or carboxylation, improve their dispersibility, increase the electroactive surface area, and enhance electrocatalytic performance [17–19]. However, the electroactive surface area of electrochemical sensors prepared solely using functionalized MWCNTs modified electrodes remains limited, and their catalytic performance is insufficient for the sensitive detection of electrochemical signals from cells. Therefore, composite materials combining MWCNTs with other nanomaterials are necessary. Nano-iron (III) oxide ($\alpha$-$Fe_2O_3$) is a transition metal oxide nanomaterial that exhibits high specific surface area, good chemical stability, and biocompatibility compared to conventional iron materials [20,21]. The combination of MWCNTs and $\alpha$-$Fe_2O_3$ is anticipated to increase the number of active reaction sites, thereby enhancing electrocatalytic performance and electron transfer efficiency. Conventional glassy carbon electrodes based on MWCNTs and $\alpha$-$Fe_2O_3$ have been successfully used for the electrochemical detection of certain environmental pollutants and drugs, such as benzoquinone, catechol, and ivabradine [22,23].

In this study, the cost-effective pencil graphite electrode (PGE) with a diameter of 2 mm was chosen as the substrate. Carboxylated multi-walled carbon nanotubes (MWCNT-COOH)/$\alpha$-$Fe_2O_3$ composite materials were synthesized using a simple green methodology, and MWCNT-COOH/$\alpha$-$Fe_2O_3$/PGE materials were prepared via a drop-coating technique. A cell-based electrochemical sensor was constructed using human hepatocellular carcinoma (HepG2) cells as a model. The MWCNT-COOH/$\alpha$-$Fe_2O_3$ composite materials were characterized using scanning electron microscopy (SEM), energy-dispersive X-ray spectroscopy (EDS), X-ray diffraction (XRD), Fourier transform infrared spectroscopy (FTIR), and cyclic

voltammetry (CV). Additionally, the cytotoxic effects of 2-CPAN, 3-CPAN, and 4-CPAN were investigated.

## 2. Materials and Methods

### *2.1. Instruments and Reagents*

2-CPAN (99%), 3-CPAN (≥98%), and 4-CPAN (≥98%) were purchased from J&K Scientific Ltd., Beijing, China. MWCNT-COOH (purity: 95%, diameter: 30–50 nm, length: 0.5–2 μm) was obtained from Jiangsu XFNANO Materials Tech Co., Ltd., Nanjing, China. $\alpha$-$Fe_2O_3$ (purity: 99.5%, particle size: 30 nm) was purchased from Aladdin Reagents Co., Ltd., Shanghai, China. PGE (type: 2 B, diameter: 2 mm) was obtained from Shanghai M&G Stationery Inc., Shanghai, China. Fetal bovine serum (FBS), DMEM culture medium, penicillin, streptomycin, serum, and phosphate-buffered saline (PBS) were all purchased from Corning, Corning, NY, USA. HepG2 cells were obtained from the Cell Bank/Stem Cell Bank of the Chinese Academy of Sciences. The cells were cultured at 37 °C in a 5% $CO_2$ incubator in a medium containing 10% fetal bovine serum and 1% antibiotics (penicillin and streptomycin).

The morphology and structure of the MWCNT-COOH/$\alpha$-$Fe_2O_3$ composite material were characterized using SEM (Zeiss Gemini Sigma 300, Jena, Germany), EDS (Ultim Max 100, London, UK), XRD (Rigaku Dmax Ultima+, Tokyo, Japan), and FTIR (Thermo Fisher Scientific Nicolet iS20, Waltham, MA, USA). All electrochemical experiments were conducted using a CHI630e electrochemical workstation. Cell morphology was observed using an inverted biological microscope (BDS-400, Chongqing, China).

### *2.2. Preparation of MWCNT-COOH/α-$Fe_2O_3$/PGE*

The PGE was polished to a mirror finish using $Al_2O_3$ powder on a polishing cloth, followed by thorough cleaning with double-distilled water and air drying. A 5 μL drop of MWCNT-COOH aqueous dispersion containing 80% (*v*/*v*) N,N-dimethylformamide (DMF) was applied to the surface of the PGE and dried under an infrared lamp to obtain MWCNT-COOH/PGE. A suitable amount of $\alpha$-$Fe_2O_3$ powder was then added to the 0.8 mg/mL MWCNT-COOH aqueous dispersion and subjected to ultrasonic treatment for 30 min. A 5 μL drop of the MWCNT-COOH/$\alpha$-$Fe_2O_3$ dispersion was subsequently applied to the polished surface of a PGE and dried under an infrared lamp to yield MWCNT-COOH/$\alpha$-$Fe_2O_3$/PGE.

### *2.3. Construction and Condition Optimization of Electrochemical Sensor*

The three-electrode system is composed of MWCNT-COOH/$\alpha$-$Fe_2O_3$/PGE as the working electrode, a saturated calomel electrode as the reference electrode, and a platinum electrode as the counter electrode. Using chronoamperometry, an enrichment time of 300 s was set, and the enrichment potentials were as follows: −0.3 V, −0.1 V, 0 V, +0.1 V, and +0.3 V. The influence of enrichment potentials on the peak current of HepG2 cells was investigated to establish the optimal enrichment conditions. The same electrode was used to continuously measure the same concentration of HepG2 cell samples ten times, and the relative standard deviation (RSD) of the oxidation peak current was calculated to evaluate the repeatability of the electrochemical sensor. Based on the optimized detection conditions, an electrochemical sensor based on MWCNT-COOH/$\alpha$-$Fe_2O_3$/PGE was constructed. Prior to its first use, the prepared MWCNT-COOH/$\alpha$-$Fe_2O_3$/PGE was scanned for 15 cycles in a 0.2 M PBS using cyclic voltammetry (CV) within a voltage range of 0 to +0.8 V.

### *2.4. Cytotoxicity Detection*

Cells were cultured in an environment maintained at 37 °C and 5% $CO_2$. To support the growth and proliferation of HepG2 cells, DMEM complete medium supplemented with 10% fetal bovine serum was utilized. To ensure cell viability and optimal growth conditions, passaging was conducted every two days. Prior to the toxicity testing, HepG2 cells were allowed a 6 h period to grow and adhere, ensuring their adaptation to the new culture environment and enabling stable proliferation. To evaluate the toxic effects of different concentrations of drinking water disinfection by-products on HepG2 cells, three sets of parallel experiments were established. The control group consisted of untreated culture medium, while the experimental groups were exposed to different concentrations of drinking water disinfection by-products: 2-CPAN (125.89 μM, 251.19 μM, 501.19 μM, 1000.00 μM, 1995.26 μM), 3-CPAN (125.89 μM, 251.19 μM, 501.19 μM, 1000.00 μM, 1995.26 μM), and 4-CPAN (125.89 μM, 251.19 μM, 501.19 μM, 1000.00 μM, 1995.26 μM).

After 36 h of cell cultivation, the culture dishes were removed for subsequent cell lysis and electrochemical detection. After PBS (pH 7.4) was added to the culture dishes, they were heated in a 50 °C constant temperature water bath for 0.5 h to promote the lysis of HepG2 cells, thereby preparing the HepG2 cells lysate. The electrochemical signals of the HepG2 cells lysate were detected using MWCNT-COOH/α-$Fe_2O_3$/PGE. The cytotoxicity was calculated using the following Formula (1) [24]:

$$Cytotoxicity = \left[\left(I_{pa,1} - I_{pa,2}\right)/I_{pa,1}\right] \times 100\% \quad (1)$$

where $I_{pa,1}$ and $I_{pa,2}$ represent the peak current values for the control group and the experimental group cells, respectively. The half inhibitory concentration ($IC_{50}$) was calculated using this formula to compare the toxic effects.

## 3. Results and Discussion

### *3.1. Characterization of MWCNT-COOH/α-$Fe_2O_3$ Composite*

The morphology of α-$Fe_2O_3$, MWCNT-COOH, and MWCNT-COOH/α-$Fe_2O_3$ was characterized using SEM (Figure 1). α-$Fe_2O_3$ exhibited a rod-like structure with a particle size of less than 30 nm (Figure 1A), while MWCNT-COOH had an intertwined tubular structure (Figure 1B) [25,26]. After the two materials were combined, α-$Fe_2O_3$ can be clearly observed to be loaded on the surface of MWCNT-COOH, indicating the successful preparation of the MWCNT-COOH/α-$Fe_2O_3$ binary nanocomposite (Figure 1C).

The elemental composition of the MWCNT-COOH/α-$Fe_2O_3$ composite was analyzed using EDS (Figure 2). Peaks attributed to C, O, and Fe elements were detected at 0.25 keV, 0.58 keV, and 0.72 keV in the EDS spectrum. The layered EDS mapping images indicate a uniform distribution of C, O, and Fe, confirming the successful preparation of the MWCNT-COOH/α-$Fe_2O_3$ composite.

The crystal structures of MWCNT-COOH, α-$Fe_2O_3$, and MWCNT-COOH/α-$Fe_2O_3$ were characterized using XRD (Figure 3A). In the spectrum of MWCNT-COOH, two peaks appeared at 2θ = 25.82° and 2θ = 42.59°, corresponding to the (002) crystal plane of the graphite-like structure and the (100) crystal plane of the periodic structure of the carbon nanotube graphene layer, respectively [27]. The α-$Fe_2O_3$ spectrum reveals several sharp characteristic peaks attributed to α-$Fe_2O_3$, indicating a relatively high degree of crystallinity [28]. In the MWCNT-COOH/α-$Fe_2O_3$ spectrum, the characteristic diffraction peaks of both MWCNT-COOH and α-$Fe_2O_3$ are present and show no significant shifts, confirming the successful formation of the composite material.

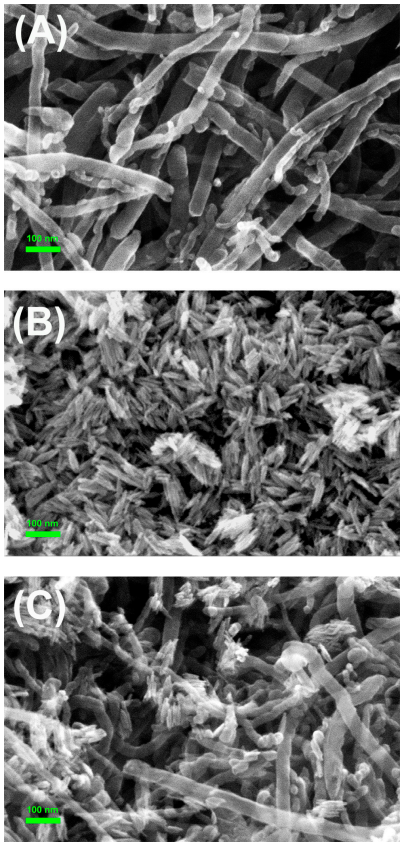


**Figure 1.** SEM images of α-$Fe_2O_3$ (**A**), MWCNT-COOH (**B**), and MWCNT-COOH/α-$Fe_2O_3$ (**C**).

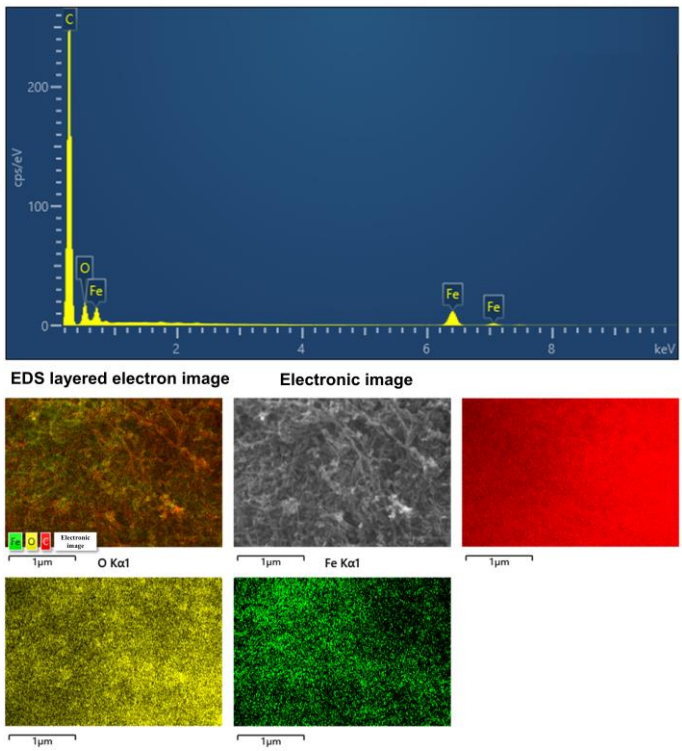


**Figure 2.** EDS spectrum of MWCNT-COOH/α-$Fe_2O_3$.

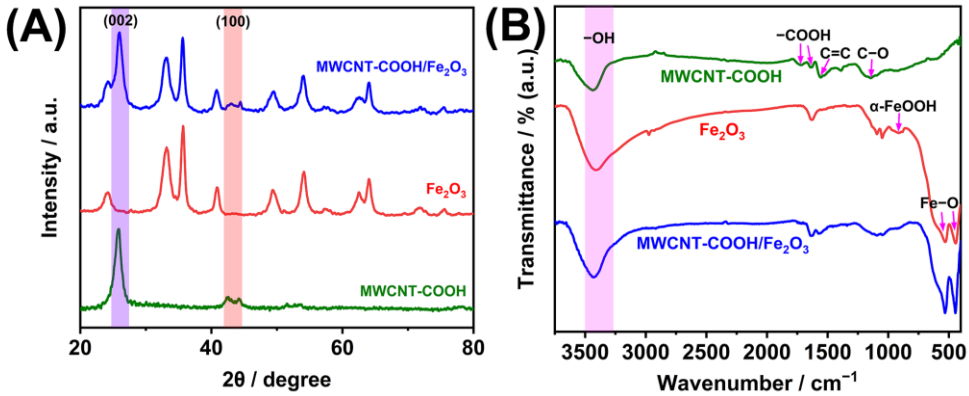


**Figure 3.** XRD (**A**) and FTIR spectra (**B**) of MWCNT-COOH, α-$Fe_2O_3$, and MWCNT-COOH/α-$Fe_2O_3$.

FTIR analysis was conducted to examine the surface functional groups of MWCNT-COOH, α-$Fe_2O_3$, and the MWCNT-COOH/α-$Fe_2O_3$ composite (Figure 3B). The FTIR spectrum of MWCNT-COOH reveals absorption peaks at 3432, 1725, 1641, and 1068 $cm^{-1}$, corresponding to the functional groups -OH, -COOH, C = C, and C-O, respectively [29,30]. In the spectrum of α-$Fe_2O_3$, characteristic vibration peaks for Fe-O were observed at 440 and 530 $cm^{-1}$, along with an absorption peak for α-FeOOH at 915 $cm^{-1}$; these findings confirm the rhombohedral crystal structure of the α-$Fe_2O_3$, specifically identifying it as α-$Fe_2O_3$ [31,32]. The spectrum of MWCNT-COOH/α-$Fe_2O_3$ exhibited the characteristic absorption peaks of both MWCNT-COOH and α-$Fe_2O_3$ without the emergence of any new peaks, indicating the successful synthesis of the MWCNT-COOH/α-$Fe_2O_3$ nanocomposite.

### *3.2. Optimization of Preparation Conditions for MWCNT-COOH/α-$Fe_2O_3$/PGE*

When preparing modified electrodes using the drop-coating method, the quantity of modifying material plays a crucial role in determining the performance of the electrochemical sensor. In previous studies [13], it has been confirmed that the electrochemical signals generated by HepG2 cells in the 0–0.8 V range are attributable to xanthine and guanine. Therefore, the impact of various concentrations (0.2, 0.4, 0.6, 0.8, and 1.0 mg/mL) of 5 μL of MWCNT-COOH on the oxidation peak current of xanthine and guanine was investigated (Figure S1A). The findings indicated that the oxidation peak current for xanthine and guanine was maximized at a concentration of 0.8 mg/mL of MWCNT-COOH in the prepared MWCNT-COOH/PGE electrode. Consequently, we selected 0.8 mg/mL as the optimal concentration for subsequent modifications of the materials.

Additionally, the ratio of composite materials significantly influences the performance of the modified electrode. Under the optimal preparation conditions for MWCNT-COOH/PGE, we explored the ideal composite ratio of α-$Fe_2O_3$ to MWCNT-COOH by varying their mass ratios (0.125, 0.5, 1.0, 1.5, 2.0). The results demonstrated that the maximum purine oxidation peak current occurred at a mass ratio of 1.5 (α-$Fe_2O_3$ to MWCNT-COOH) (Figure S1B), indicating optimal performance of the MWCNT-COOH/α-$Fe_2O_3$/PGE composite. Therefore, a mass ratio of 1.5 for α-$Fe_2O_3$ to MWCNT-COOH was determined to be the optimal condition for synthesizing MWCNT-COOH/α-$Fe_2O_3$/PGE.

### *3.3. Construction of Cell Electrochemical Sensor Based on MWCNT-COOH/α-$Fe_2O_3$/PGE*

The differential pulse voltametric behavior of HepG2 cells ($1.0 \times 10^6$ cells/mL) on the composite-modified electrode MWCNT-COOH/α-$Fe_2O_3$/PGE was investigated (Figure 4). A weak oxidation peak was detected at +0.63 V on PGE, with a peak current of 1.29 μA (Figure 4A). After modification with MWCNT-COOH, the oxidation peak current at MWCNT-COOH/PGE increased to 2.18 μA, and the oxidation peak potential shifted to +0.60 V, attributed to the intrinsic excellent electron transfer capability and outstanding

electrocatalytic performance of MWCNT-COOH (Figure 4B). Following the addition of $\alpha$-$Fe_2O_3$, the oxidation peak current at MWCNT-COOH/$\alpha$-$Fe_2O_3$/PGE further increased to 3.47 µA, with a slight decrease in oxidation peak potential by 0.005 V to +0.595 V compared to MWCNT-COOH/PGE (Figure 4C). This improvement is due to the good catalytic performance of $\alpha$-$Fe_2O_3$, and the synergistic effect between $\alpha$-$Fe_2O_3$ and MWCNT-COOH enhances the conductivity of $\alpha$-$Fe_2O_3$. Figure 4D displays a comparative graph of the signals obtained from the cell lysate using the three types of electrodes after baseline correction, facilitating the observation of changes in the oxidation peak current across different electrodes.

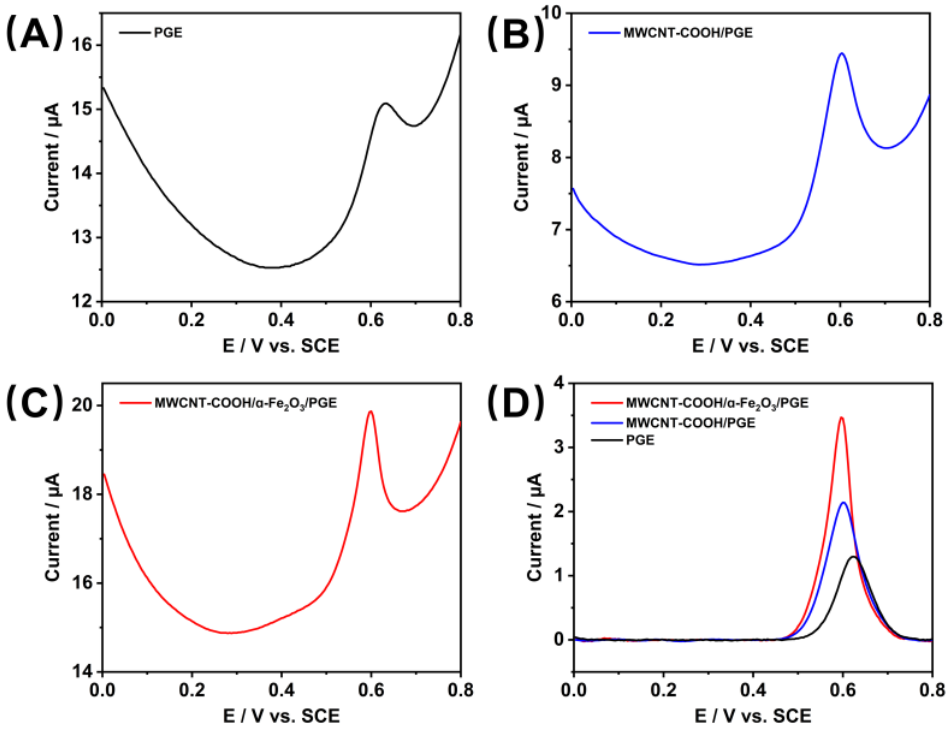


**Figure 4.** Differential pulse voltammetry of HepG2 cell lysate on (**A**) PGE, (**B**) MWCNT-COOH/PGE, and (**C**) MWCNT-COOH/$\alpha$-$Fe_2O_3$/PGE and (**D**) baseline corrected differential pulse voltammetry of different electrodes in HepG2 cell lysate (Initial potential: 0 V; final potential: 0.8 V; voltage increment: 0.004 V; amplitude: 0.05 V pulse width: 0.05 s; sampling width: 0.0167 s; pulse period: 0.5 s; quiet time: 2 s).

The influence of various enrichment potentials on the oxidation peak current of HepG2 cells was analyzed (Figure 5A). At negative potentials, the measured electrochemical signal intensity decreased. At an enrichment potential of 0 V or positive values, there was no significant effect on the electrochemical signal. Higher enrichment potentials may lead to increased background electrochemical reactions, generating background signals that interfere with the detection of the target analytes. Therefore, 0 V was chosen as the enrichment potential for detecting HepG2 cells using MWCNT-COOH/$\alpha$-$Fe_2O_3$/PGE. The reproducibility of the electrode was assessed by measuring HepG2 cells ten consecutive times with the same MWCNT-COOH/$\alpha$-$Fe_2O_3$/PGE (Figure 5B). The relative standard deviation (RSD) of the measured electrical signal was found to be 2.03%, indicating that the prepared MWCNT-COOH/$\alpha$-$Fe_2O_3$/PGE exhibits good reproducibility.

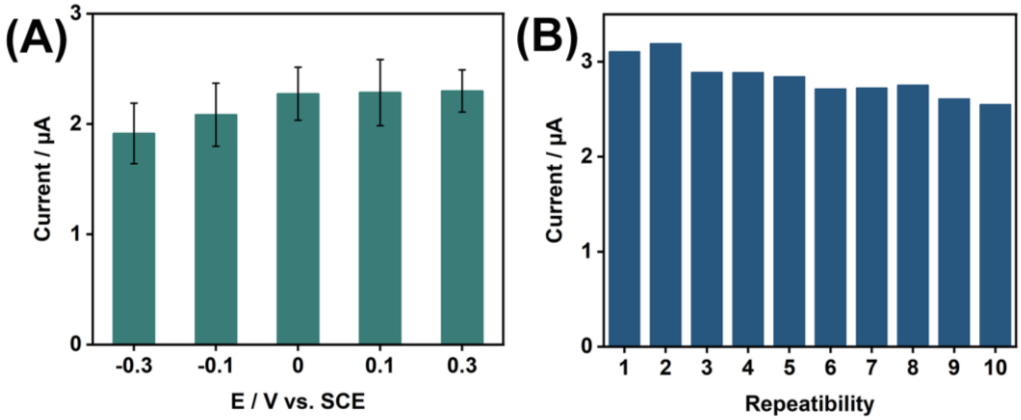


**Figure 5.** (**A**) Effect of enrichment potential on electrochemical signals of HepG2 cells detected by MWCNT-COOH/α-$Fe_2O_3$/PGE. (**B**) Repeatability of MWCNT-COOH/α-$Fe_2O_3$/PGE (Cell density: $1 \times 10^6$ cells $mL^{-1}$).

### *3.4. Evaluation of the Toxicity of DBPs on HepG2 Cells*

The constructed electrochemical sensor based on MWCNT-COOH/α-$Fe_2O_3$/PGE was utilized to study the cytotoxicity of three chlorophenyl acetonitrile DBPs (Figure S2 and Figure 6). Linear regression was performed on the logarithm of concentration versus cell toxicity to calculate the $IC_{50}$ values for HepG2 cells (Table 1). All three DBPs exhibited cytotoxicity, with $IC_{50}$ values of 831.76, 812.83, and 660.69 μM for 3-CPAN, 4-CPAN, and 2-CPAN, respectively. Studies on the cytotoxic mechanisms of various aromatic DBPs indicate that oxidative stress is one of the significant mechanisms leading to cytotoxicity [33]. The intracellular levels of reactive oxygen species (ROS) can partially reflect the extent of oxidative stress. The production of ROS, along with the imbalance in cellular redox state, can trigger excessive ROS production, resulting in destructive impacts on lipids, proteins, and DNA, ultimately leading to cell death [34]. Additionally, interactions between exogenous substances and the antioxidant enzyme system have also been confirmed as a mechanism of toxicity [35]. For example, exposure of cells to halogenated aromatic DBPs for a period results in a significant reduction in intracellular glutathione (GSH) levels [36]. Some DBPs can directly bind with GSH to form various glutathione conjugates, further reducing intracellular GSH levels [37]. GSH and the glutathione peroxidase enzyme system play crucial roles in the pathways of cellular redox homeostasis, and a decrease in GSH levels can weaken the cellular resistance to oxidative stress, increasing the risk of cell damage and death.

**Table 1.** The linear equation between the concentration logarithm ($X$) of different DBPs and their cytotoxicity ($Y$) and their $IC_{50}$ values to HepG2 cells.

| Toxicant | Signal | $IC_{50}$ |
|---|---|---|
| 2-CPAN | $Y = 35.61\ X - 55.43$ (r = 0.976) | 660.69 μM |
| 3-CPAN | $Y = 31.58\ X - 39.88$ (r = 0.962) | 831.76 μM |
| 4-CPAN | $Y = 36.90\ X - 61.61$ (r = 0.916) | 812.83 μM |

The order of cytotoxicity of chlorophenyl acetonitrile-type DBPs is 2-CPAN (ortho) > 4-CPAN (para) > 3-CPAN (meta). 2-CPAN (ortho) exhibits the strongest toxic effect on HepG2 cells, possibly due to the proximity of the chlorine atom to the cyano group, which affects the electronic density of the benzene ring and enhances the reactivity of the cyano group. This increased reactivity may lead to stronger interactions with biomacromolecules (such as proteins and DNA), thereby increasing cytotoxicity. The toxic effect of 4-CPAN (para) on HepG2 cells is higher than that of 3-CPAN (meta), which is consistent with the

toxicity patterns of halogenated phenolic quinone-type DBPs in Chinese hamster ovary cells, where the cytotoxicity of 2,5-para-quinone is greater than that of 2,6-meta-quinone [38]. Research on the reactivity and genotoxicity of halophenolquinone isomers on DNA in human hepatocytes indicates that the dipole moment is a key structural parameter affecting DNA reactivity, cytotoxicity, and genotoxicity of HBQ isomers. The value of the dipole moment indicates the average distribution of charge and electrons within the molecule, and the reactivity of the molecule is strongly influenced by the dipole moment, with asymmetric molecules having a higher dipole moment than symmetric ones [39]. This may explain why the toxicity of 4-CPAN is greater than that of 3-CPAN.

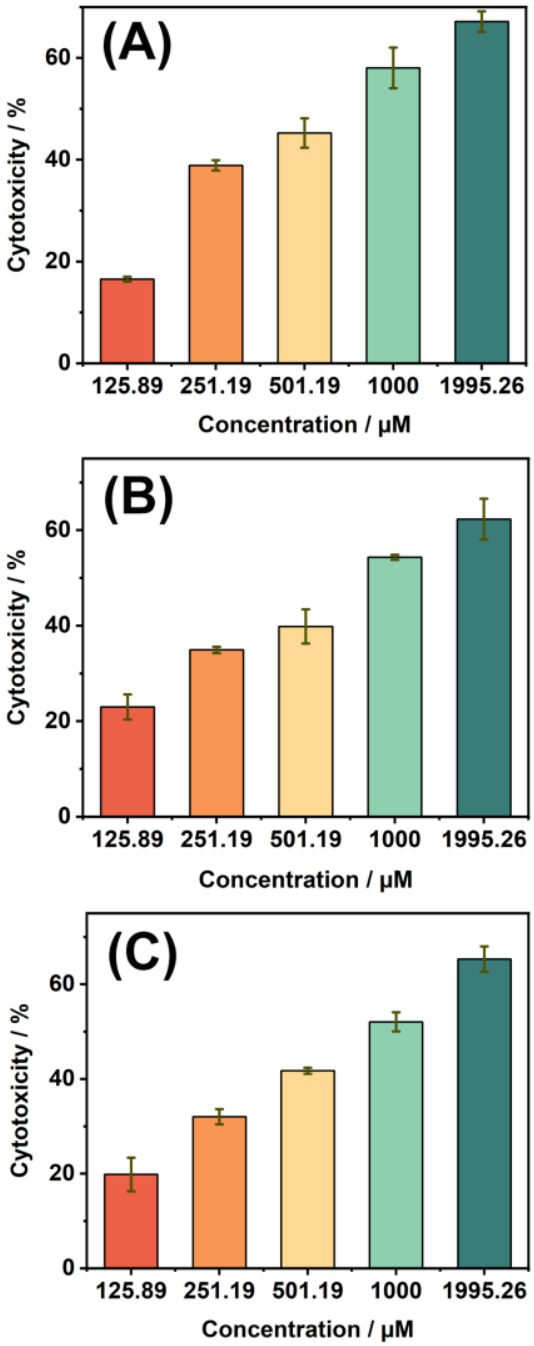


**Figure 6.** Cytotoxicity of 2-CPAN (**A**), 3-CPAN (**B**), and 4-CPAN (**C**) to HepG2 cells detected by the electrochemical sensor.

The changes in the morphology of HepG2 cells after exposure to chlorophenyl acetonitrile-type DBPs were studied (Figures 7–9). With increasing concentrations of

pollutants, the cell density gradually decreased. Most HepG2 cells in the control group displayed a spindle shape (Figures 7A, 8A and 9A), whereas the morphology of HepG2 cells after exposure showed significant changes, with cells becoming smaller and rounder, along with the appearance of numerous contracted dead cells (Figures 7B–F, 8B–F and 9B–F), indicating that all three chlorophenyl acetonitrile-type DBPs can inhibit the activity of HepG2 cells.

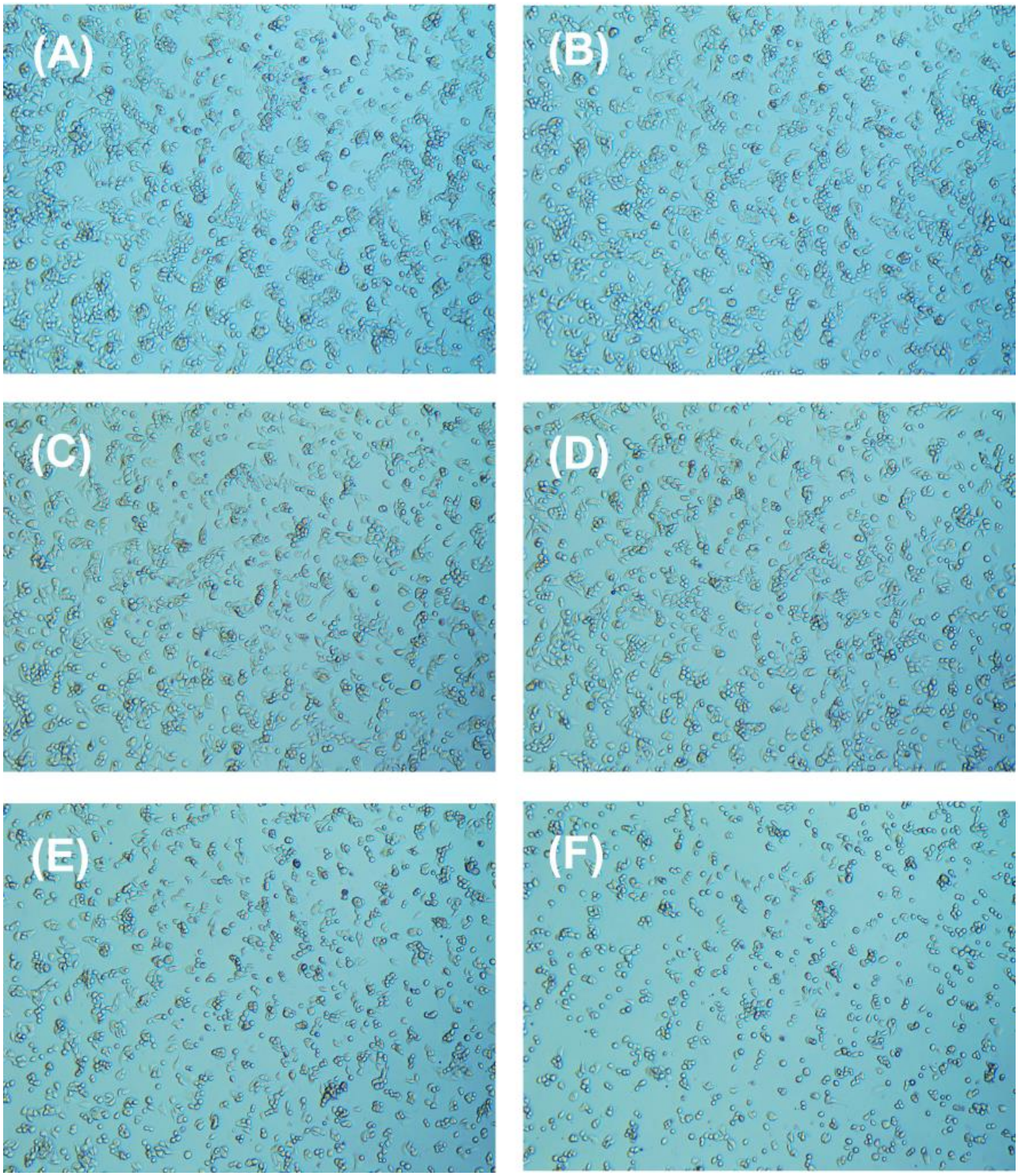


**Figure 7.** Cellular morphology of HepG2 cells (**A**) before and after treatment with (**B**) 125.89 μM, (**C**) 251.19 μM, (**D**) 501.19 μM, (**E**) 1000.00 μM, and (**F**) 1995.26 μM 2-CPAN for 36 h.

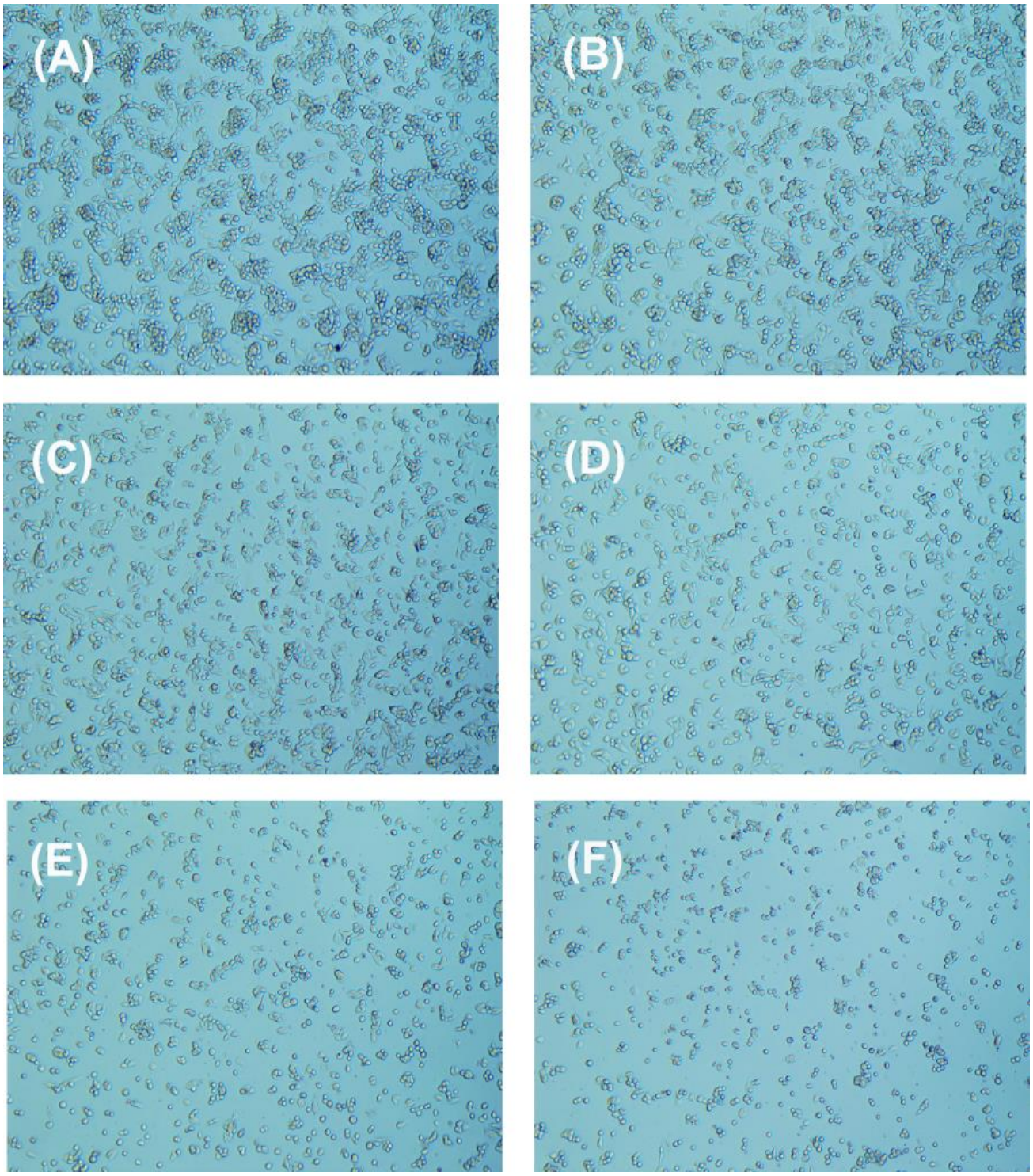


**Figure 8.** Cellular morphology of HepG2 cells (**A**) before and after treatment with (**B**) 125.89 μM, (**C**) 251.19 μM, (**D**) 501.19 μM, (**E**) 1000.00 μM, and (**F**) 1995.26 μM 3-CPAN for 36 h.

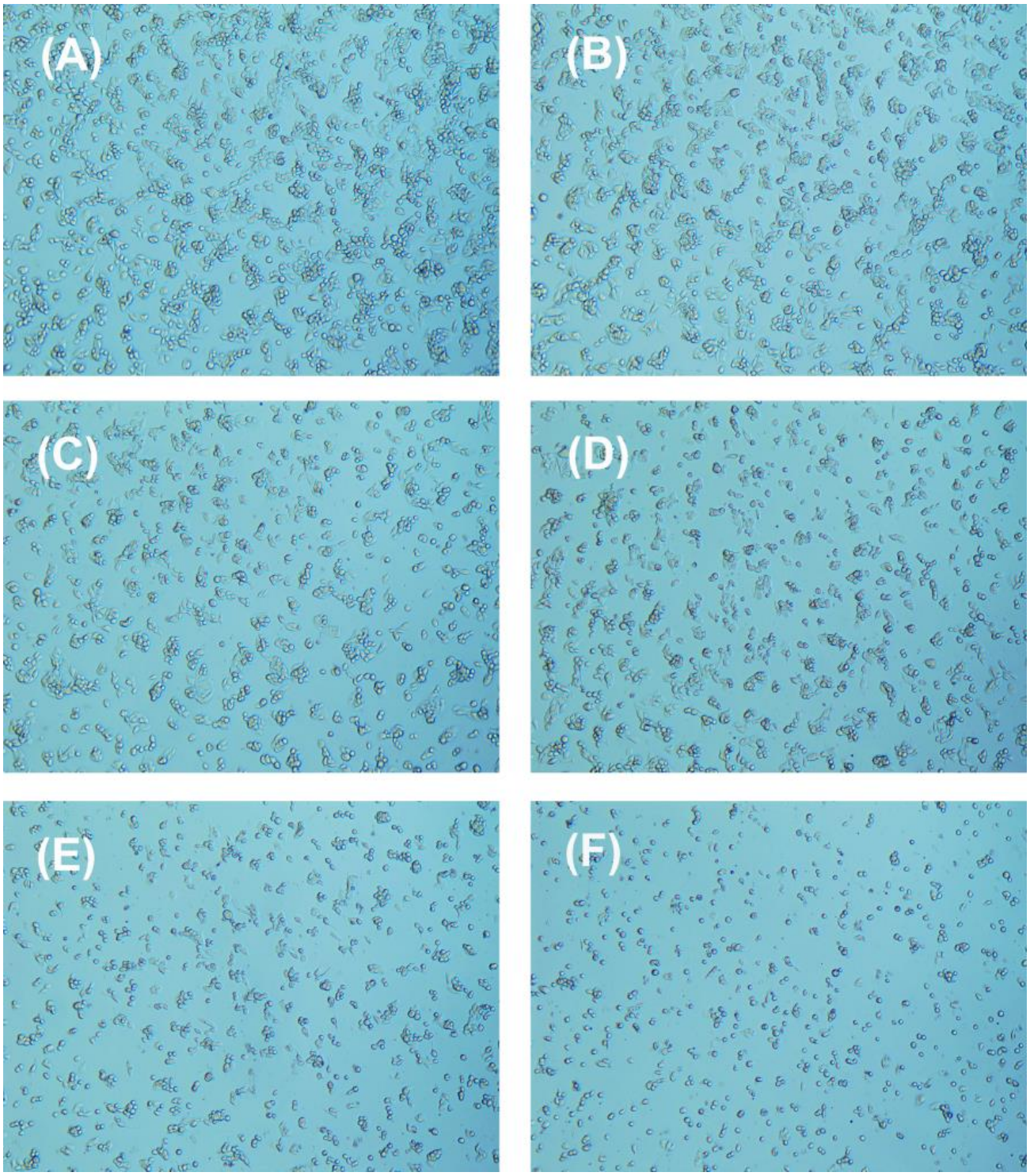


**Figure 9.** Cellular morphology of HepG2 cells (**A**) before and after treatment with (**B**) 125.89 μM, (**C**) 251.19 μM, (**D**) 501.19 μM, (**E**) 1000.00 μM, and (**F**) 1995.26 μM 4-CPAN for 36 h.

## 4. Conclusions

In this study, we developed an electrochemical cell sensor utilizing MWCNT-COOH/$\alpha$-$Fe_2O_3$/PGE, showcasing excellent electrocatalytic performance. Compared to traditional cell toxicity detection methods, the electrochemical cell sensor has advantages such as simplicity, speed, and being label-free. Furthermore, the pencil graphite electrodes used in this study are only one-thousandth the cost of conventional glassy carbon elec-

trodes, significantly reducing research costs. We investigated the toxicity of DBPs including 2-CPAN, 3-CPAN, and 4-CPAN based on changes in the electrochemical signals of HepG2 cells. Our findings indicate that 2-CPAN exhibits the highest level of toxicity to HepG2 cells, followed by 4-CPAN, while 3-CPAN demonstrates the lowest level of toxicity. Changes in cell morphology also reflect the varying toxicity levels associated with different types and concentrations of DBPs. This study provides technical support and scientific evidence for the detection of toxicity and the safety assessment of DBPs in water environments. In addition to cytotoxicity detection, the sensor can also be promoted and applied in other fields for detecting cellular nucleotide metabolic products, such as assessing cellular metabolic function and studying drug performance.

**Supplementary Materials:** The following supporting information can be downloaded at https://www.mdpi.com/article/10.3390/nano15020146/s1: Figure S1. Oxidation peak current diagram of 20 μM xanthine/guanine mixture at (A) MWCNT-COOH/PEG and (B) MWCNT-COOH/α-$Fe_2O_3$/PEG. Figure S2. The oxidation peak current values of cell lysates corresponding to different concentrations of (A) 2-CPAN, (B) 3-CPAN, and (C) 4-CPAN.

**Author Contributions:** Conceptualization, J.Q. and X.Z.; Methodology, Y.L. and Z.Z.; Validation, Z.Z.; Investigation, Y.L., Z.Z., Y.W. and H.Y.; Writing—original draft, Y.L.; Writing—review & editing, X.Z.; Supervision, X.Z.; Funding acquisition, J.Q. and X.Z. All authors have read and agreed to the published version of the manuscript.

**Funding:** This work was supported by the National Natural Science Foundation of China (42177371, 51809044, and 42130705).

**Data Availability Statement:** Data are contained within the article and Supplementary Materials.

**Conflicts of Interest:** The authors declare no conflict of interest.

## References

1. Liu, X.; Chen, L.; Yang, M.; Tan, C.; Chu, W. The occurrence, characteristics, transformation and control of aromatic disinfection by-products: A review. *Water Res.* **2020**, *184*, 116076. [CrossRef] [PubMed]
2. Zhang, Z.; Zhu, Q.; Huang, C.; Yang, M.; Li, J.; Chen, Y.; Yang, B.; Zhao, X. Comparative cytotoxicity of halogenated aromatic DBPs and implications of the corresponding developed QSAR model to toxicity mechanisms of those DBPs: Binding interactions between aromatic DBPs and catalase play an important role. *Water Res.* **2020**, *170*, 115283. [CrossRef] [PubMed]
3. Jiang, L.; Luo, J.; Wei, W.; Song, M.; Shi, W.; Li, A.; Zhou, Q.; Pan, Y. Comparative cytotoxicity analyses of disinfection byproducts in drinking water using dimensionless parameter scaling method: Effect of halogen substitution type and number. *Water Res.* **2023**, *240*, 120087. [CrossRef] [PubMed]
4. Dong, Y.; Qiang, Z.; Richardson, S.D. Formation of iodinated disinfection byproducts (I-DBPs) in drinking water: Emerging concerns and current issues. *Accounts Chem. Res.* **2019**, *52*, 896–905. [CrossRef] [PubMed]
5. Wagner, E.D.; Plewa, M.J. CHO cell cytotoxicity and genotoxicity analyses of disinfection by-products: An updated review. *J. Environ. Sci.* **2017**, *58*, 64–76. [CrossRef]
6. Zhang, D.; Bond, T.; Li, M.; Dong, S.; Pan, Y.; Du, E.; Xiao, R.; Chu, W. Ozonation treatment increases chlorophenylacetonitrile formation in downstream chlorination or chloramination. *Environ. Sci. Technol.* **2021**, *55*, 3747–3755. [CrossRef]
7. Zhang, D.; Chu, W.; Yu, Y.; Krasner, S.W.; Pan, Y.; Shi, J.; Yin, D.; Gao, N. Occurrence and stability of chlorophenylacetonitriles: A new class of nitrogenous aromatic DBPs in chlorinated and chloraminated drinking waters. *Environ. Sci. Technol. Lett.* **2018**, *5*, 394–399. [CrossRef]
8. Zhang, D.; Bond, T.; Krasner, W.S.; Chu, W.; Pan, Y.; Xu, B.; Yin, D. Trace determination and occurrence of eight chlorophenylacetonitriles: An emerging class of aromatic nitrogenous disinfection byproducts in drinking water. *Chemosphere* **2018**, *220*, 858–865. [CrossRef] [PubMed]
9. Zhu, W.; Zhang, Y.; Wang, J.; Liu, W.; Wang, H.; Song, M.; Zhang, H.; Wang, X. In situ monitoring of toxic effects of algal toxin on cells by a novel microfluidic flow cytometry instrument. *Ecotox. Environ. Safe* **2024**, *270*, 115894. [CrossRef]
10. Bhatt, B.S.; Gandhi, D.H.; Vaidya, F.U.; Pathak, C.; Patel, T.N. Cell apoptosis induced by ciprofloxacin based Cu(II) complexes: Cytotoxicity, SOD mimic and antibacterial studies. *J. Biomol. Struct. Dyn.* **2020**, *39*, 4555–4562. [CrossRef] [PubMed]
11. Wu, D.; Fu, G.; Wang, J.; Ge, L.; Zhu, J.; Yuan, X.; Liu, J. Voltammetric behavior of the heat-treating PC-3 cells and its application in drug sensitivity test. *Electrochem. Commun.* **2011**, *13*, 623–626. [CrossRef]

12. Sun, H.; Zheng, H.; Zhang, Z.; Liu, Y.; Qu, J.; Zhu, X. Cytotoxicity assessment of nanoplastics and associated additives using an electrochemical sensor based on carbon nanohorn/gold nanoparticles. *J. Environ. Chem. Eng.* **2023**, *11*, 111452. [CrossRef]
13. Zhou, S.; Xing, Y.; Yuan, X.; Wu, G.; Zhu, X.; Wu, D. Cytotoxicity and action mechanisms of polycyclic aromatic hydrocarbons by a miniature electrochemical detection system. *Biomed. Microdevices* **2021**, *23*, 19. [CrossRef] [PubMed]
14. Zhu, X.; Zheng, H.; Zhang, Z.; Ma, S.; Feng, Q.; Wang, J.; Wu, G.; Ng, H.Y. Cytotoxicity evaluation of organophosphorus flame retardants using electrochemical biosensors and elucidation of associated toxic mechanisms. *Water Res.* **2024**, *265*, 122262. [CrossRef]
15. Özcan, A.; Şahin, Y. A novel approach for the selective determination of tryptophan in blood serum in the presence of tyrosine based on the electrochemical reduction of oxidation product of tryptophan formed in situ on graphite electrode. *Biosens. Bioelectron.* **2012**, *31*, 26–31. [CrossRef]
16. Zhu, X.; Wu, G.; Lu, N.; Yuan, X.; Li, B. A miniaturized electrochemical toxicity biosensor based on graphene oxide quantum dots/carboxylated carbon nanotubes for assessment of priority pollutants. *J. Hazard. Mater.* **2017**, *324*, 272–280. [CrossRef]
17. Domínguez, A.A.; Dominguez, R.B.; Zaragoza, C.E.A. Simultaneous detection of dihydroxybenzene isomers using electrochemically reduced graphene oxide-carboxylated carbon nanotubes/gold nanoparticles nanocomposite. *Biosensors* **2021**, *11*, 321. [CrossRef] [PubMed]
18. Indah, W.N.; Tawatchai, K.; Rodtichoti, W.; Proespichaya, K.; Panote, T.; Warakorn, L. Electrochemical sensor based on molecularly imprinted polymer cryogel and multiwalled carbon nanotubes for direct insulin detection. *Talanta* **2023**, *254*, 124137. [CrossRef]
19. Guo, X.; Wang, Q.; Li, J.; Cui, J.; Zhou, S.; Hao, S.; Wu, D. A mini-electrochemical system integrated micropipet tip and pencil graphite electrode for detection of anticancer drug sensitivity in vitro. *Biosens. Bioelectron.* **2015**, *64*, 594–596. [CrossRef] [PubMed]
20. Juthi, A.; Mohammad, R.; Lynn, D.; Uddin, A.M. Electrochemiluminescence nanoimmunosensor for CD63 protein using a carbon nanochips/iron oxide/nafion-nanocomposite modified mesoporous carbon interface. *Measurement* **2020**, *170*, 108755. [CrossRef]
21. Wang, F.; Yang, J.; Li, S.; Liang, J.; Wang, Y.; Du, R.; Zhou, B.; Liu, Q.; Li, C. Constructing ultralow-loading Cu single atoms/$Fe_2O_3$ particles on $Nb_2C$ MXenes for efficient utilization of atomic H to boost electrochemical debromination. *Chem. Eng. J.* **2024**, *498*, 155550. [CrossRef]
22. Sawczuk, R.B.S.; Pinheiro, H.A.; Santos, J.R.N.; Alves, I.C.B.; Viegas, H.D.C.; Lacerda, C.A.; Sousa, J.K.C.; Marques, E.P.; Marques, A.L.B. A sensitive electrochemical nanosensor based on iron oxide nanoparticles and multiwalled carbon nanotubes for simultaneous determination of benzoquinone and catechol in groundwater. *Int. J. Environ. Anal. Chem.* **2023**, *103*, 1733–1750. [CrossRef]
23. Abdel-Haleem, F.M.; Gamal, E.; Rizk, M.S.; Madbouly, A.; El Nashar, R.M.; Anis, B.; Elnabawy, H.M.; Khalil, A.S.G.; Barhoum, A. Molecularly imprinted electrochemical sensor-based $Fe_2O_3$@MWCNTs for ivabradine drug determination in pharmaceutical formulation, serum, and urine samples. *Front. Bioeng. Biotechnol.* **2021**, *9*, 648704. [CrossRef] [PubMed]
24. Xing, Y.; Zheng, H.; Wang, C.; Zhang, Z.; Qian, Y.; Qu, J.; Zhu, X. Cost-efficient and ultrasensitive sensor for electrochemical detection and cytotoxicity assessment of tetracyclines. *J. Environ. Chem. Eng.* **2024**, *12*, 113642. [CrossRef]
25. Cao, T.T.; Phan, N.D.D.; Pham, V.T.; Nguyen, T.H.; Nguyen, V.T.; Cao, T.A.; Pham, V.H.; Kanako, Y.; Hiroya, A.; Nguyen, V.C. 3D porous graphene/double-walled carbon nanotubes/gold nanoparticles hybrid film for modifying electrochemical electrode. *Mater. Lett.* **2023**, *330*, 133308. [CrossRef]
26. Patta, S.; Suryasnata, T.; Rama, K.V.S.; Govind, S.S. Label-free, ultrasensitive and rapid detection of FDA-approved TBI specific UCHL1 biomarker in plasma using MWCNT-PPY nanocomposite as bio-electrical transducer: A step closer to point-of-care diagnosis of TBI. *Biosens. Bioelectron.* **2022**, *216*, 114631. [CrossRef]
27. Zhang, Z.; Zheng, H.; Liu, Y.; Ma, S.; Feng, Q.; Qu, J.; Zhu, X. Highly sensitive detection of multiple antiviral drugs using graphitized hydroxylated multi-walled carbon nanotubes/ionic liquids-based electrochemical sensors. *Environ. Res.* **2024**, *249*, 118466. [CrossRef] [PubMed]
28. Devi, S.; Tripta; Ankita; Kumar, S.; Kumar, R.; Kumar, V.; Kumar, A.; Singh, O.; Kumar, P. Efficient α–$Fe_2O_3$@NiO nanocomposites as a photocatalyst for the treatment of hazardous Rose Bengal dye. *Phys. Rev. B Condens.* **2025**, *696*, 416649. [CrossRef]
29. Solhy, A.; Machado, B.F.; Beausoleil, J.; Kihn, Y.; Gonçalves, F.; Pereira, M.F.R.; Órfão, J.J.M.; Figueiredo, J.L.; Faria, J.L.; Serp, P. MWCNT activation and its influence on the catalytic performance of Pt/MWCNT catalysts for selective hydrogenation. *Carbon* **2008**, *46*, 1194–1207. [CrossRef]
30. Shaqayeq, A.; Hamid, M. Removal of carboxylated multi-walled carbon nanotubes (MWCNT-COOH) from the environment by Trametes versicolor: A simple, cost-effective, and eco-friendly method. *Sci. Rep.* **2023**, *13*, 16139. [CrossRef]
31. Sharma, R.; Kumar, H.; Saini, C.; Gupta, A.; Pandit, V. Exploring the collaborative wonders of $Al_2O_3$-$Mn_3O_4$-$Fe_2O_3$ nanoparticles embedded in reduced graphene oxide matrices. *Inorg. Chem. Commun.* **2024**, *162*, 112275. [CrossRef]
32. Ghaffar, S.; Ahmed, A.; Jamshaid, M.; Al-onazi, W.A.; Ali, M.A.; Iqbal, A.; Iqbal, R. Construction of visible-light-induced $Fe_2O_3$/g-$C_3N_4$ nanocomposites for the enhanced degradation of organic dyes: Optimization of operative parameters. *Polyhedron* **2024**, *264*, 117254. [CrossRef]

33. Klaunig, J.E.; Kamendulis, L.M.; Hocevar, B.A. Oxidative stress and oxidative damage in carcinogenesis. *Toxicol. Pathol.* **2010**, *38*, 96–109. [CrossRef] [PubMed]
34. Mao, Y.; Ai, H.; Chen, Y.; Zhang, Z.; Zeng, P.; Kang, L.; Li, W.; Gu, W.; He, Q.; Li, H. Phytoplankton response to polystyrene microplastics: Perspective from an entire growth period. *Chemosphere* **2018**, *208*, 59–68. [CrossRef]
35. Li, J.; Wang, W.; Zhang, H.; Le, X.C.; Li, X.-F. Glutathione-mediated detoxification of halobenzoquinone drinking water disinfection byproducts in T24 cells. *Toxicol. Sci.* **2014**, *141*, 335–343. [CrossRef] [PubMed]
36. Wang, W.; Qian, Y.; Li, J.; Aljuhani, N.; Siraki, A.G.; Le, X.C.; Li, X. Characterization of mechanisms of glutathione conjugation with halobenzoquinones in solution and HepG2 cells. *Environ. Sci. Technol.* **2018**, *52*, 2898–2908. [CrossRef]
37. Subramanian, K.; Iovino, F.; Tsikourkitoudi, V.; Merkl, P.; Ahmed, S.; Berry, S.B.; Aschtgen, M.S.; Svensson, M.; Bergman, P.; Sotiriou, G.A.; et al. Mannose receptor-derived peptides neutralize pore-forming toxins and reduce inflammation and development of pneumococcal disease. *Embo Mol. Med.* **2020**, *12*, 12695. [CrossRef] [PubMed]
38. Li, J.; Moe, B.; Vemula, S.; Wang, W.; Li, F. Emerging disinfection byproducts, halobenzoquinones: Effects of isomeric structure and halogen substitution on cytotoxicity, formation of reactive oxygen species, and genotoxicity. *Environ. Sci. Technol.* **2016**, *50*, 6744–6752. [CrossRef] [PubMed]
39. Tu, N.; Liu, H.; Li, W.; Yao, S.; Liu, J.; Guo, Z.; Yu, R.; Du, H.; Li, J. Quantitative structure-toxicity relationships of halobenzoquinone isomers on DNA reactivity and genotoxicity. *Chemosphere* **2022**, *309*, 136763. [CrossRef] [PubMed]